Sources of possible artefacts in the contrast evaluation for the backscattering polarimetric images of different targets in turbid medium

Tatiana Novikova, Arnaud Bénière, François Goudail, Antonello de Martino

Sources of possible artefacts in the contrast evaluation for the backscattering polarimetric images of different targets in turbid medium

**Tatiana Novikova,[1,*] Arnaud Bénière,[2] François Goudail,[2]
and Antonello De Martino[1]**

[1] LPICM, Ecole polytechnique, CNRS, Palaiseau 91128, France
[2] Institut d'Optique Graduate School, Palaiseau 91127, France
[*]tatiana.novikova@polytechnique.edu

Abstract: It is known that polarization-sensitive backscattering images of different objects in turbid media may show better contrasts than usual intensity images. Polarimetric image contrast depends on both target and background polarization properties and typically involves averaging over groups of pixels, corresponding to given areas of the image. By means of numerical modelling we show that the experimental arrangement, namely, the shape of turbid medium container, the optical properties of the container walls, the relative positioning of the absorbing, scattering and reflecting targets with respect to each other and to the container walls, as well as the choice of the image areas for the contrast calculations, can strongly affect the final results for both linearly and circularly polarized light.

References and links

1. G. D. Lewis, D. L. Jordan, and P. J. Roberts, "Backscattering target detection in a turbid medium by polarization discrimination," Appl. Opt. **38**(18), 3937–3944 (1999).
2. G. W. Kattawar, and M. J. Raković, "Virtues of mueller matrix imaging for underwater target detection," Appl. Opt. **38**(30), 6431–6438 (1999).
3. R. Nothdurft, and G. Yao, "Expression of target optical properties in subsurface polarization-gated imaging," Opt. Express **13**(11), 4185–4195 (2005), http://www.opticsinfobase.org/oe/abstract.cfm?URI=oe-13-11-4185.
4. R. E. Nothdurft, and G. Yao, "Effects of turbid media optical properties on object visibility in subsurface polarization imaging," Appl. Opt. **45**(22), 5532–5541 (2006).
5. S. G. Demos, and R. R. Alfano, "Optical polarization imaging," Appl. Opt. **36**(1), 150–155 (1997).
6. S. G. Demos, H. Radousky, and R. Alfano, "Deep subsurface imaging in tissues using spectral and polarization filtering," Opt. Express **7**(1), 23–28 (2000), http://www.opticsinfobase.org/oe/abstract.cfm?URI=oe-7-1-23.
7. H. Shao, Y. He, Y. Shao, and H. Ma, "Contrast enhancement subsurface optical imaging with different incident polarization states", Proc. of SPIE, **6047**, 60470Z(1–6), (2006).
8. G. C. Giakos, A. Molhokar, A. Orozco, V. Kumar, S. Sumrain, D. Mehta, A. Maniyedath, N. Ojha, and A. Medithe, "Laser imaging through scattering media", IMTC 04. Proc. of the 21st IEEE, **1,** 433 - 437 (2004).
9. F. C. MacKintosh, J. X. Zhu, D. J. Pine, and D. A. Weitz, "Polarization memory of multiply scattered light," Phys. Rev. B **40**(13), 9342–9345 (1989).
10. G. Yao, "Differential optical polarization imaging in turbid media with different embedded objects," Opt. Commun. **241**(4-6), 255–261 (2004).
11. P. W. Zhai, G. W. Kattawar, and P. Yang, "Mueller matrix imaging of targets under an air-sea interface," Appl. Opt. **48**(2), 250–260 (2009).
12. S. Huard, *The Polarization of Light* (Wiley, New York, 1997).
13. R. A. Chipman, "Polarimetry" in *Handbook of Optics*, 2nd ed. M. Bass ed. (McGraw Hill, New York, 1995), vol. 2, chap 22.
14. G. I. Bell, and S. Glasstone, *Nuclear Reactor Theory* (Van Nostrand Reinhold, New York, 1970).
15. B. Kaplan, G. Ledanois, and B. Drévillon, "Mueller matrix of dense polystyrene latex sphere suspensions: measurements and monte carlo simulation," Appl. Opt. **40**(16), 2769–2777 (2001).
16. R. Kalibjian, "Stokes polarization vector and Mueller matrix for a corner-cube reflector," Opt. Commun. **240**(1-3), 39–68 (2004).
17. H. C. Van de Hulst, *Light scattering by Small Particles* (Dover, New York, 1981).

1. Introduction

Subsurface polarization imaging of different objects in turbid media has been intensively studied in different fields such as target detection, ocean optics, medical imaging and diagnostics [1–8]. The enhancement of image optical contrast provided by various polarimetric imaging techniques (Mueller matrix, differential polarization, degree of polarization…) was evaluated by comparison with standard intensity imaging.

Before undertaking polarimetric studies of complex systems of practical interest (e.g. air-ocean or human tissues) many researchers start with measurements on laboratory samples. Most frequently the model turbid media used in laboratory experiments are particle suspensions placed in containers with limited dimensions. Such measurements are used, for example, to determine which state of polarization – linear or circular – provides better image contrast with orthogonal state contrast (OSC) imaging. It was reported [9] that circularly polarized light tends to better preserve its original state of polarization in the backscattered light compared to the linearly polarized light after multiple scattering if the size of scattering particles is larger than the wavelength of light. As Mueller matrix describes both linearly and circularly polarized light interaction with any sample, we focused our study on the simulation of full backscattering Mueller matrices.

The influence of both the target and the background optical properties (scattering and absorption coefficients, anisotropy) on the target visibility was experimentally studied in [3,4]. The effectiveness of target discrimination in a scattering medium with both circularly and linearly polarized light was investigated experimentally [1,7] and numerically [10]. The effects of ruffled air-water interface and the finite size of the active light source on the underwater target detection were studied in [11].

In such experiments, due attention is devoted to the most important parameters; i.e. the target depth, the scattering and absorption mean free paths and the scattering anisotropy. Conversely, the other geometrical parameters such as the shape and the transverse dimensions of the turbid medium container, the optical properties of the container walls, the relative positions of the targets (in case of multiple targets) and their distance to the container walls are usually considered irrelevant and they are not reported. The main purpose of this work is to demonstrate that these parameters may also strongly affect the polarimetric image contrast, an effect which is almost always overlooked.

The paper is organized as follows. In section 2 we reformulate the basics of Mueller-Stokes formalism, we briefly summarize the Monte-Carlo numerical technique applied for the solution of the vector radiative transfer equation and describe the typical measurement set-up used for the simulations. In Section 3 the results of these simulations are presented and discussed. Section 4 concludes the paper.

2. Methods

2.1 Mueller-Stokes Formalism

As long as only intensities are measured the results of any classical measurement are defined by the second moments (quadratic quantities) of the electric field distributions. In the field of linear optics any partially polarized electric field is fully characterized by its four dimensional Stokes vector **S** defined, for any set of orthogonal axes (x, y), as:

$$\mathbf{S} = \begin{pmatrix} I \\ Q \\ U \\ V \end{pmatrix} = \begin{pmatrix} I_x + I_y \\ I_x - I_y \\ I_{45°} - I_{-45°} \\ I_L - I_R \end{pmatrix} = \begin{pmatrix} < E_x E_x^* + E_y E_y^* > \\ < E_x E_x^* - E_y E_y^* > \\ < E_x E_y^* + E_y E_x^* > \\ i < E_x E_y^* - E_y E_x^* > \end{pmatrix}, \quad (1)$$

where I_x, I_y, $I_{+45°}$, $I_{-45°}$ are the intensities which would be measured after passing through linear polarizers oriented along the x, y, $+45°$ and $-45°$ respectively in the plane perpendicular to the direction of wave propagation, while I_L and I_R would be the intensities transmitted by left and

right circular polarizers, and E_x, E_y are two orthogonal components of complex Jones vector of the electric field [12]. The Stokes vector is thus defined in terms of directly measurable intensities, which is not the case for the electric field amplitudes involved in the Jones formalism.

In the most general case of partially polarized light the brackets at the right hand side of Eq. (1) stand for all possible ways to take averages, e.g. spatially, spectrally or temporally, depending on the sample and the measurement conditions. Thus partially polarized states can be viewed as incoherent superposition of fully polarized states with different polarizations.

Within the Stokes formalism, the degree of polarization ρ_s related to a given Stokes vector **S** is defined as:

$$\rho_{\mathbf{S}} = \frac{\sqrt{Q^2 + U^2 + V^2}}{I} \quad (0 \le \rho_{\mathbf{S}} \le 1). \tag{2}$$

This quantity varies between 0 (totally depolarized states) and 1 (totally polarized states).

As the Stokes vector is directly related to intensities, upon interaction with any sample it undergoes a linear transformation, described by a 4×4 real matrix **M**, called the Mueller matrix of the sample [12,13]:

$$\mathbf{S}^{out} = \mathbf{M}\,\mathbf{S}^{in}. \tag{3}$$

Due to the capability of the Stokes vectors to describe any polarization state, the Mueller matrix can fully describe the polarimetric properties of any sample, be it depolarizing or not. Depending on whether the overall transmission (or reflectivity) of the sample is of interest or not, the Mueller matrix may be considered in its original (non-normalized) or normalized form ($M_{ij}* = M_{ij} / M_{11}$).

2.2 Numerical Technique

The propagation of the polarized light in a turbid media is described by the linear vector radiative transfer equation

$$\frac{1}{c}\frac{\partial \mathbf{S}(\mathbf{r},\mathbf{\Omega},t)}{\partial t} + \mathbf{\Omega} \cdot \nabla \mathbf{S}(\mathbf{r},\mathbf{\Omega},t) = \int_{4\pi} \mu_{sca}(\mathbf{r})\mathbf{M}(\mathbf{\Omega}' \to \mathbf{\Omega}) \cdot \mathbf{S}(\mathbf{r},\mathbf{\Omega}',t)d\mathbf{\Omega}' - \mu_{T}(\mathbf{r})\mathbf{S}(\mathbf{r},\mathbf{\Omega},t) + \mathbf{Q}_{ext}(\mathbf{r},\mathbf{\Omega},t) \tag{4}$$

where $\mathbf{S}(\mathbf{r},\mathbf{\Omega},t)$ represents the Stokes vector of the light at the space point **r**, direction $\mathbf{\Omega}$ and time *t*, $\mathbf{M}(\mathbf{\Omega}' \to \mathbf{\Omega})$ is the 4×4 phase matrix, representing at point **r** the probability of the of light propagating in direction $\mathbf{\Omega}'$ to be scattered in the direction $\mathbf{\Omega}$, $\mathbf{Q}_{ext}$ is the contribution of the external photon sources, μ_T = $N\sigma_T$ and μ_{sca} = $N\sigma_{sca}$ are the total and scattering attenuation coefficients, σ_T and σ_{sca} are the total and scattering cross-sections of single particle respectively, N is a number density of the particles. The integro-differential Eq. (4) can be transformed by the method of characteristics [14] to the integral inhomogeneous Fredholm equation of the second kind:

$$\mathbf{S} = K[\mathbf{S}] + \mathbf{Q}', \tag{4a}$$

where *K* is the scattering integral and **Q**' is the contribution of the external photon sources. In general no analytical solution is available for Eq. (4a), so we applied the numerical Monte Carlo technique to evaluate *K*. This statistical approach allowed to solve the problem in realistic (sometimes quite complex) experimental configurations, with straightforward physical interpretation of the results.

The incident light beam was treated as a flux of photons undergoing the elastic collisions within the turbid medium and Fresnel refraction and reflection on the interfaces. We made use of two main physical assumptions: 1) the scattering was independent, the mean free path of photon was much longer than the wavelength of the light and 2) the scattering was incoherent,

with direct addition of scattered intensities, as is the case for classical sources, due to their very small coherence lengths.

The initial state of polarization of each photon was chosen on the Poincaré sphere:

$$\mathbf{S}_{in}(\alpha,\beta) = (1, \ \cos\alpha, \ \sin\alpha \cdot \cos\beta, \ \sin\alpha \cdot \sin\beta)^{\mathrm{T}}, \qquad (5)$$

where α and β are random numbers uniformly distributed over $[0, \pi]$ and $[0, 2\pi]$ respectively. The Stokes vector and space coordinates of each propagating photon were traced statistically. The Stokes vector of the photon reaching the detector is described by

$$\mathbf{S}_{out}(\alpha,\beta) = \mathbf{M} \cdot \mathbf{S}_{in}(\alpha,\beta), \qquad (6)$$

where $\mathbf{M}$ is the Mueller matrix of the sample under study and the value of $\mathbf{S}_{in}(\alpha,\beta)$ is defined from Eq. (5). Since the components of the Stokes vector are orthogonal functions, it follows from Eq. (6) that

$$\int_0^\pi \int_0^{2\pi} \left(\mathbf{M} \cdot \mathbf{S}_{in}(\alpha,\beta) \right) \cdot \mathbf{S}_{in}(\alpha,\beta)^{\mathrm{T}} \, d\alpha \, d\beta = \mathbf{M} \cdot \mathbf{D}, \qquad (7)$$

where $\mathbf{D}$ is 4×4 diagonal matrix with elements $D_i = \int_0^\pi \int_0^{2\pi} \left[\mathbf{S}_{in}^i(\alpha,\beta) \right]^2 d\alpha \, d\beta$, which were calculated analytically. The integration of the double integral on the left side of Eq. (7) was also performed by Monte Carlo technique. A standard deviation of normalized Mueller matrix coefficients smaller than 1.5% was chosen as the criterion of the algorithm convergence. The detailed description of the algorithm can be found elsewhere [15].

2.2 Modelled set-up

The basic set-up for numerical experiment is presented in Fig. 1. A container of square cross section filled with the monodispersed suspension of 1 µm diameter polystyrene latex spherical particles in water was defined as the sample for calculations (see Fig. 1(a)).

We took the dimensions of plastic container which was used in the laboratory for the experiments with backscattering polarimetric imaging: depth of 16.4 cm and lateral dimensions 9 cm $\times$ 9 cm.

Mie theory calculations give an anisotropy factor $g = 0.917$ and a scattering coefficient $\mu_s = 0.734$ cm^{-1} for 1 µm diameter polystyrene particle in water. The concentration of particles was fixed at $3.6 \cdot 10^7$ particles/cm^3 to ensure the transport mean free path (mfp') $l_s' = 1/(\mu_s (1-g)) = 16.4$ cm be equal to the depth of container. Due to the large value of anisotropy factor the enhancement of forward light scattering with small fraction of light to be scattered back was expected within the container volume. Consequently, one would not expect that the lateral dimensions of the container, which were smaller than transport mean free path l_s' but larger than mean free path $l_s = 1/\mu_s = 1.36$ cm, would have any significant influence on the backscattering polarimetric image of the sample.
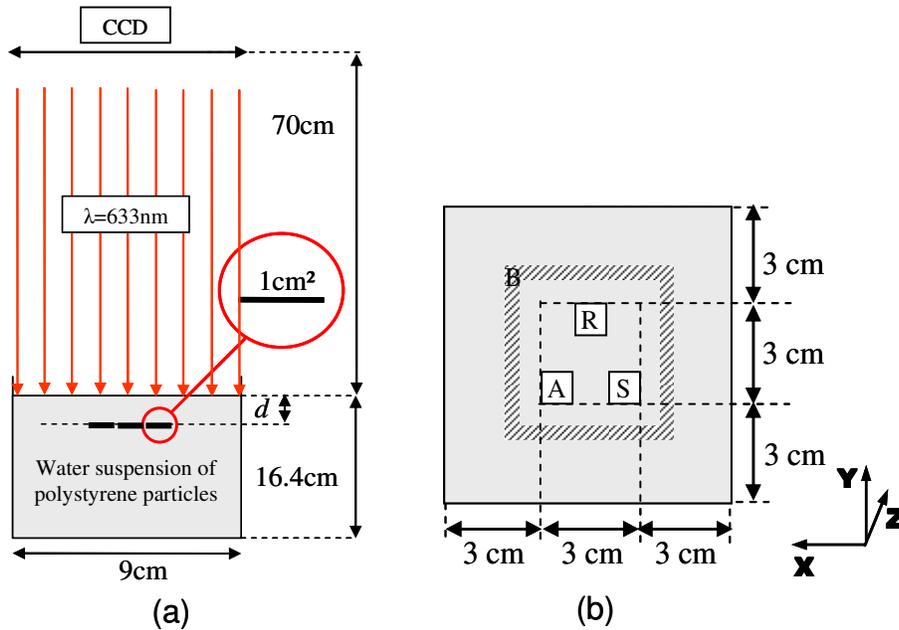
Fig. 1. The schematic of modelled set-up (a). Target immersion depth d was varied from 0.1 cm till 8.2 cm (0.006 mfp'-0.5 mfp'). Top view of the sample and laboratory coordinate system (b). Letters (**R**), (**A**) and (**S**) are for reflecting (mirror), absorbing and scattering targets, respectively. Scattering background properties were averaged over the dashed area (**B**) (see text).

Different optical properties were assigned to the container walls (completely absorbing or transparent 0.5 mm thick plastic walls) in order to study the effects of container boundaries. The collimated polarized light source with the wavelength of 633 nm was normally incident upon the sample top surface and illuminated it uniformly. At this wavelength the refractive indices of polystyrene spheres and water are $n_p = 1.59$ and $n_{water} = 1.33$ respectively, with vanishing imaginary part (no absorption). The distance from the backscattered light detector to the surface of the sample was fixed at 70 cm.

Three types of square (1×1 cm^2) targets were immersed into the suspension of polystyrene particles in water (see Fig. 1(b), top view). Similar target configuration was used for the polarimetric imaging of the combined multiple targets in [4]. The reflecting target R was considered to be an aluminium mirror ($n_R = 1.21 + i \cdot 6.93$), the Mueller matrix of the dielectric-metal interface was calculated according to [16]. The absorbing target A was modelled as perfect absorber and scattering target S - as a diffusively reflecting (lambertian) surface. The immersion depth of the targets was varied from 0.1 to 8.2 cm with respect to the air-water interface. The detector provided the images of full Mueller matrix of the sample top surface with the resolution of 90×90 pixels. The size of single pixel was chosen to be 1 mm^2 in order to reduce the statistical noise of calculations.

As long as differential polarization imaging is performed it is common [3–5,7,8] to define the measured orthogonal state contrast (OSC) as

$$OSC = \frac{I_{co} - I_{cr}}{I_{co} + I_{cr}}, \quad (8)$$

where I_{co} and I_{cr} represent co-polarized and cross-polarized light intensities with respect to the incident beam. For an incident linearly-horizontal polarized beam I_{co} is the intensity of backscattered light at horizontal detection, I_{cr} is the intensity at vertical detection. When an incident beam is right-circularly polarized, I_{co} is the intensity of backscattered light at

clockwise detection and I_{cr} is the intensity at counter-clockwise detection. As follows from Eq. (1), (3) and (8) the OSC values for linearly and circularly polarized light can be expressed in terms of Mueller matrix coefficients:

$$OSC_L = \frac{M_{22} + M_{21}}{M_{11} + M_{12}}, \tag{9}$$

$$OSC_C = \frac{M_{44} + M_{41}}{M_{11} + M_{14}}, \tag{10}$$

if we define a linearly-horizontal polarized beam to be parallel to the x axis of the laboratory coordinate system. The corresponding OSC_L and OSC_C values were calculated for each pixel (i, j) of the images taken at different target immersion depths.

The spatial averaging for OSC_L^{tar} and OSC_C^{tar} values was performed over the pixels (i, j) from T - central quarter of the area of each target. The values of OSC_L^b and OSC_C^b for the scattering background were calculated using the pixels (i, j) from B - 0.5 cm width stripe, surrounding target area (see Fig. 1b).

$$OSC_L^{tar\,(b)} = \frac{\left\langle M_{22}^{ij} + M_{21}^{ij} \right\rangle}{\left\langle M_{11}^{ij} + M_{12}^{ij} \right\rangle}, \quad OSC_C^{tar\,(b)} = \frac{\left\langle M_{44}^{ij} + M_{41}^{ij} \right\rangle}{\left\langle M_{11}^{ij} + M_{14}^{ij} \right\rangle}, \quad (i,j) \in T\,(B). \tag{11}$$

3. Results and discussion

3.1 Mutual impact of multiple targets

The backscattering Mueller matrix images of the sample with the parameters defined in section II were calculated at different target immersion depths. Since the contribution of photons reflected specularly on the air-water interface without entering scattering medium was the same for all the pixels, this contribution was subtracted from the images.

First we defined the container walls as completely absorbing. The Mueller matrix diagonal elements M_{11}, $M_{22}*$, $M_{33}*$ and $M_{44}*$ are presented in Fig. 2. All calculated off-diagonal elements of Mueller matrix were about three orders of magnitude less than diagonal elements, i. e. they were statistically equal to zero. This means that the sample behaved as a pure depolarizer. The values of $M_{22}*$ were almost everywhere equal to the absolute values of $M_{33}*$, as expected for an isotropic medium [17].

The unpolarized backscattering images of the sample (M_{11} upper row, Fig. 2) show that the visibility of the absorbing target drops faster with immersion depth than that of the reflecting and scattering targets. With the chosen scattering coefficient μ_s and combined target configuration the absorbing target becomes almost invisible on the unpolarized intensity images when the immersion depth d exceeds critical value of $0.24 \cdot l_s'$. The same tendency is observed in the polarimetric images ($M_{22}*$, $M_{33}*$ and $M_{44}*$ rows in Fig. 2) but the absorbing target image fades even faster (critical value $d = 0.18 \cdot l_s'$).

The reflecting and scattering targets send some light back at different angles, and thus they perturb the values of Mueller matrix coefficients for background medium in the target surrounding areas. As there is no light coming back from the absorbing target, the light scattered by background medium next to absorbing target masks the absorbing target response. This explains why the absorbing target image is smaller than the reflecting and scattering target images.
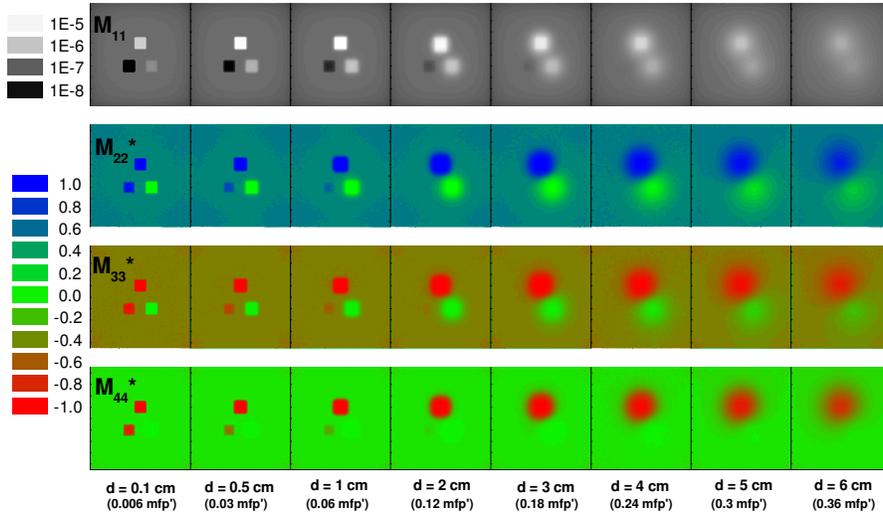
Fig. 2. Backscattering 9×9 cm^2 simulated images of diagonal Mueller matrix coefficients of the sample at different target immersion depth. M_{11} is the reflectance of the sample (logarithmic scale). All walls of the container are completely absorbing.

At a certain depth the polarimetric response of the absorbing target is shadowed by the broadening cone of the light reflected by the mirror target. This effect of mutual target impact on a polarimetric image, which depends on the target configuration, will be discussed below. With the increase of immersion depth the scattering target shows better visibility in linearly polarized images ($M_{22}*$ and $M_{33}*$ rows in Fig. 2) compared with circular polarized image ($M_{44}*$ row, Fig. 2).

The values of OSC_L and OSC_C calculated with Eqs. (9)-(11) for the reflecting, absorbing, scattering targets and surrounding turbid background are presented in Fig. 3 versus target immersion depth expressed in a transport mean free path l_s'.

For all targets and scattering background the OSC_L value is higher then OSC_C value at any target immersion depth. Despite the multiple scattering of the light within the container volume (mean free path $l_s = 1.36$ cm), due to the high anisotropy factor g the scattered light direction is slowly randomized. Consequently the frame of reference for the linear polarized eigenvectors remains almost unchanged, thus preserving the OSC_L values after short path backscattering sequences. At the same time the flip of helicity of the backscattered circularly polarized light affects the OSC_C values significantly. Both linear and circular OSC values of the reflecting and scattering targets show opposite trends with increasing depth.

The values of OSC decrease for reflecting target and increase for scattering target, asymptotically approaching the OSC values of scattering background (see Fig. 3(a), (b)). The values of OSC_L and OSC_C of absorbing target show non-monotonous variation with the immersion depth increase (see Fig. 3(c), solid symbols). To understand this phenomenon we repeated the calculations with the same parameters but without reflecting and scattering targets.
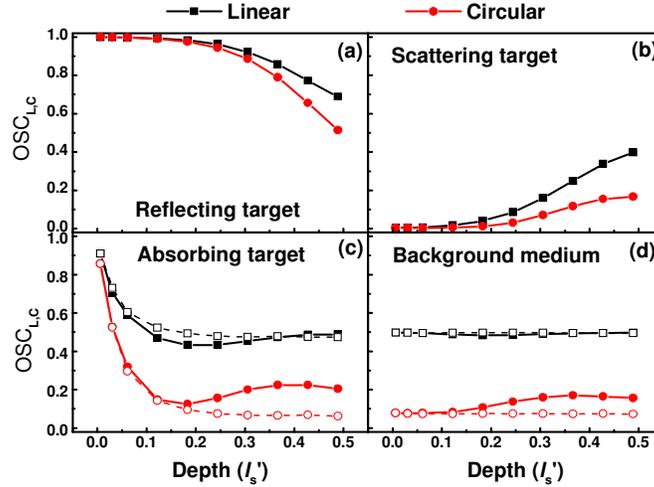
Fig. 3. Linear and circular OSC values of (a) reflecting, (b) scattering, (c) absorbing targets and (d) background versus target depth immersion (l_s'). Open symbols (see 3(c) and 3(d)) show the values of $OSC_{L,C}$ when scattering and reflecting targets were removed. All walls of the container are completely absorbing.

With only absorbing target immersed the values of OSC_L and OSC_C decrease monotonously with the immersion depth (see Fig. 3(c), open symbols). For example, at $d = 0.18 \cdot l_s'$ the value of OSC_L of the single absorbing target increases and the value of OSC_C decreases (see Fig. 3(c), open symbols) because we removed the shadowing of the absorbing target by the backscattering light cone of scattering target (see Fig. 2, M_{22}^* and M_{44}^* rows).

Usually the values of OSC of both target and background are involved in image contrast calculations

$$\text{Contrast} = \left| OSC_k^{\text{tar}} - OSC_k^{\text{b}} \right| \Big/ \left(OSC_k^{\text{tar}} + OSC_k^{\text{b}} \right), \quad k = L,C. \qquad (12)$$

At $d > 0.3 \cdot l_s'$ both OSC_L and OSC_C values of single absorbing target were equal to the corresponding values for scattering background (see Fig. 3(c), (d), open symbols), hence, according to Eq. (12) single absorbing target in turbid medium was invisible at depths larger than $0.3 \cdot l_s'$.

For multiple targets at larger immersion depths the broadening of light cone backscattering from the reflecting target perturbed the calculated apparent value of OSC_C of scattering background (see Fig. 2, (M_{44}^* row) and Fig. 3(d) (solid symbols)). The calculated value of scattering background OSC_L remained almost constant, because the broadening of light cone backscattering from the reflecting target was accompanied by the broadening of light cone backscattering from the scattering target and their respective OSC_L values have an opposite trend (see Fig. 2, (M_{22}^* row) and Fig. 3(a),(b),(d)).

The impact of the boundaries on polarimetric images of the sample is clearly seen in Fig. 2. The absolute values of M_{22}^*, M_{33}^* (and OSC_L value consequently) of the scattering background are higher for the pixels in the corners of the container compared to the central part. The values of $OSC_{L,C}^{\text{b}}$ are used for image contrast evaluation, so the choice of pixels for the spatial averaging can affect the calculated image contrast.

3.2 Impact of container walls on the contrast evaluation

To study the influence of container walls on the values of OSC_L and OSC_C of the scattering background medium we performed simulations of the sample described above but without any target immersed, varying the material of the wall. First we assumed that the walls were absorbing and afterwards we modelled a container with plastic walls of 0.5 mm thickness and

$n_{wall} = 1.58$. We performed spatial averaging of simulated Mueller matrix coefficients over the pixels of whole top surface of the sample. The results are presented in Tab. 1. The simulated optical properties of the container wall and the cross-section of container in (x, y) plane are given in the first and second columns respectively.

Table 1. Normalized diagonal Mueller matrix coefficients of the scattering background medium averaged over the whole sample top surface. There were no targets immersed.

Walls of container	Container cross-section	$M_{22}*$	$M_{33}*$	$M_{44}*$
Absorbing	Square (9 cm × 9 cm)	0.49	−0.49	−0.07
Plastic 0.5 mm	Square (9 cm × 9 cm)	0.33	−0.22	−0.04
Plastic 0.5 mm	Circle (R = 4.5 cm)	0.24	−0.24	−0.05

The light reflection at water-plastic interface does not exceed 1% at normal incidence for the wavelength 633 nm. There is also contribution of the photons coming back to container volume due to the total internal reflection at plastic-air interface. Despite the small changes in the backscattered intensity the polarimetric response of the scattering background medium for the linearly polarized light changed significantly when the optical properties of the container walls were varied. The off-diagonal terms of Mueller matrix remained equal to zero, but for the container with transparent plastic walls the averaged value of diagonal element $M_{22}*$ exceeded the corresponding absolute value of $M_{33}*$ by 50% (see Tab. (1)).

It is worth to note that in general the OSC_L value calculated with Eq. (8) can depend on the orientation of the linear polarizer with respect to the (x, y) axes of the laboratory coordinate system. For example, if we define a linearly-horizontal polarized beam to be at 45° to the x axis of the laboratory coordinate system, the Eq. (9), expressing the OSC_L value in terms of Mueller matrix coefficients, transforms into

$$OSC_L = \frac{M_{33} + M_{31}}{M_{11} + M_{13}}. \tag{13}$$

The values of $OSC_L{}^b$ calculated using either Eq. (9) or Eq. (13) will be different, because $M_{22}* \neq M_{33}*$. This means that for the studied sample the orthogonal state contrast of the scattering background medium for linear polarization ($OSC_L{}^b$) is not invariant under the linear polarizer plane rotation by 45° around z axis. In the case of completely absorbing walls, there are no photons coming back from the walls to the scattering medium. When the walls of container reflect photons back to the scattering medium, the polarization of these photons contribute to the polarimetric image of the sample carrying back the information about the optical properties of the boundaries and their position with respect to the linear polarizer plane orientation. The square cross-section sample is not invariant under rotation by 45° around z axis. Thus, for given scattering coefficient μ_s the value of $OSC_L{}^b$ and, consequently, the contrast value (see Eq. (12)) for linearly polarized light will strongly depend on the orientation of linear polarizer plane with respect to the side and diagonal of the square cross-section of the sample.

To check the effect of the container shape on the contrast evaluation for the linearly polarized light we repeated the simulations for the same sample but chose the container to be a cylinder of the same depth 16.4 cm and diameter 9 cm equal to the side of square cross-section of the previous container. We took the plastic walls of cylinder of the same thickness 0.5 mm and $n_{wall} = 1.58$. The cross-section of the cylindrical container in (x, y) plane is invariant under any rotation around z axis. Consequently, due to an azimuthal symmetry of the sample the calculated averaged coefficients $M_{22}*$ and $M_{33}*$ become equal (see Tab. (1)).

4. Conclusions

We studied numerically the impact of experimental set-up design and boundary conditions on the contrast evaluation for backscattering polarimetric Mueller matrix images of different types of targets immersed in a turbid medium.

Depending on experimental set-up arrangement, scattering coefficient μ_s and transport mean free path l_s' the walls of the container can actively interfere with the scattered polarized light. The lack of sample azimuthal symmetry in (x, y) plane perpendicular to the direction of wave propagation can affect the OSC image of the sample for linearly polarized light. It can induce significant errors in the differential polarization image contrast evaluation. To avoid these errors we need to measure complete Mueller matrix of the sample or degree of polarization ρ_s of backscattering light (see Eq. (2),(3)).

The OSC_L value of the scattering background medium for the container with square cross-section depends on the exact orientation of the linear polarizer plane, being maximal for the horizontal linear-polarized light direction parallel to the walls of square cross-section and minimal when this direction is parallel to the diagonals of the square.

The value of scattering coefficient μ_s, used in our simulations was quite low. However, we believe that not the exact value of scattering coefficient (or mean free path) is important in the experiments, but rather the ratio of transport mean free path l_s' to the characteristic dimension L of the container with scattering sample. Obviously, the decrease of ratio l_s'/L will reduce the influence of the above mentioned artefacts on polarimetric image contrast. The use of point source illumination directed towards the centre of sample surface will also decrease the impact of container walls on polarimetric image contrast.

The design of multiple targets configuration can also be the source of artefacts in the polarimetric image contrast evaluation. As a rule of thumb, all potentially perturbing objects (other targets, walls…) should be placed several transport mean free paths away from the studied object to limit or avoid significant perturbations.

It is worth to mention that many experiments and simulations on the polarimetric subsurface target imaging in turbid media were focused on the optimal choice of the incident light polarization (linear versus circular) for a better image contrast. However, our simulations proved that carrying out such studies one should take care of proper experimental set-up design in order to remove the sources of possible artefacts in a polarimetric image contrast evaluation. It was also shown that at certain conditions the measurements of the complete set of data (Mueller matrix or Stokes vector) are more reliable for correct comparison of the image contrast for linearly polarized light versus circularly polarized one.

Acknowledgements